applied optics

Real-time two-dimensional beam steering with gate-tunable materials: a theoretical investigation

JIERONG CHENG, SAMAD JAFAR-ZANJANI, AND HOSSEIN MOSALLAEI*

Department of Electrical and Computer Engineering, Northeastern University, Boston, Massachusetts 02115, USA
**Corresponding author: hosseinm@ece.neu.edu*

Received 6 May 2016; revised 22 June 2016; accepted 10 July 2016; posted 11 July 2016 (Doc. ID 264690); published 1 August 2016

A leaky-wave antenna is proposed that furnishes two-dimensional (2-D) beam scanning in both elevation and azimuth planes via electrical control in real time, and at a single frequency. The structure consists of a graphene sheet on a metal-backed substrate. The 2-D beam-scanning performance is achieved through the proper biasing configuration of graphene. Traditional pixel-by-pixel electrical control makes the biasing network a huge challenge for chip-scale designs in the terahertz regime and beyond. The method presented here enables dynamic control by applying two groups of one-dimensional biasing on the sides of the sheet. They are orthogonal and decoupled, with one group offering monotonic impedance variation along one direction, and the other sinusoidal impedance modulation along the other direction. The conductivity profile of the graphene sheet for a certain radiation angle, realized by applying proper voltage to each pad underneath the sheet, is determined by a holographic technique and can be reconfigured electronically and desirably. Such innovative biasing design makes real-time control of the beam direction and beamwidth simple and highly integrated. The concept is not limited to graphene-based structures, and can be generalized to any available gate-tunable material system.

OCIS codes: (160.3918) Metamaterials; (240.6690) Surface waves; (310.6845) Thin film devices and applications; (060.4080) Modulation.

http://dx.doi.org/10.1364/AO.55.006137

1. INTRODUCTION

Antenna arrays with beam-scanning capability are essential components in wireless communications, sensing, and imaging [1,2]. The system cost can be drastically reduced if the radiation direction can be tuned dynamically and efficiently. For antenna arrays working at micro/millimeter wave frequencies, such flexibility is usually attained through independent phase control of each antenna with parasitic lumped elements, such as varactors and PIN diodes [3–5], together with the biasing network. As the frequency moves toward the terahertz (THz) and optical ranges, the profile of the pixel will be much smaller than the wavelength due to the plasmonic effect. The array ends up with thousands of elements in order to be functional and efficient in practice. One can modulate the properties of the entire array via electrical control at the edge of the active material [6,7]. However, to achieve more flexible tunability, independent electrical control pixel by pixel may be preferable. Considering the small size and the huge number of elements, the biasing network would be too complicated, and would impose stringent requirements for fabrication and integration. Few preliminary studies have been reported with dynamic control at the high-frequency range [8,9].

Recently, the emergence of gate-tunable materials, such as graphene, indium tin oxide (ITO), and vanadium oxide (VO_2), provides intriguing material platforms for reconfigurable nanoantennas and metamaterials from the THz to the infrared [10–14]. The electrical and optical properties of these thin materials can be easily tuned by DC gate biasing. Reconfigurable beam scanning toward arbitrary elevation angle has been recently proposed by proper one-dimensional (1-D) biasing distribution underneath a graphene layer [15]. Applying different voltages to different gate biasing strips underneath graphene realizes a sinusoidal surface impedance distribution, which scatters the bounded surface wave into a spatial radiation beam. By changing the modulation period through simple variation of the voltage distribution, the radiation beam can be scanned to a different direction. Nevertheless, dynamic scanning of the radiation in both the elevation and azimuth planes is of significant interest and, at the same time, very challenging, as pixel-by-pixel tuning makes

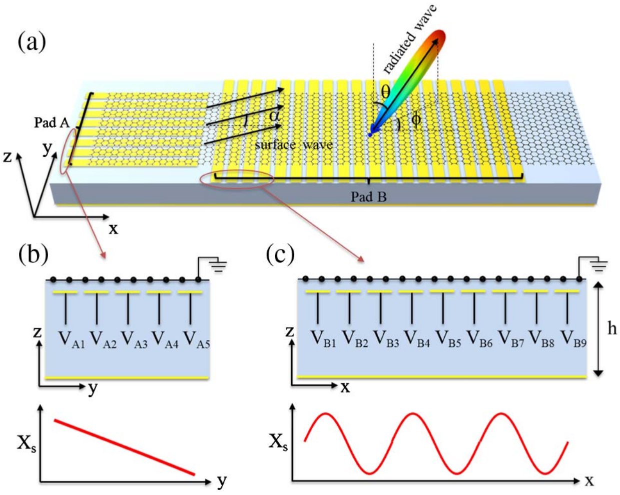

Fig. 1. (a) Schematic representation of a graphene leaky-wave antenna for dynamic beam scanning toward any spatial 2-D direction $[\theta, \phi]$. 1-D biasing pads are placed under a homogeneous graphene layer. Pad group A changes the surface wave propagation direction in the $x-y$ plane, and pad group B provides sinusoidal impedance modulation for leaky-wave generation. (b) Cross-section configuration in the area of pad group A and the monolithic impedance variation along y, achieved by pad group A. (c) Cross-section configuration in the area of pad group B and the sinusoidal impedance distribution along x, achieved by pad group B. Here, only the reactance profile is plotted by assuming pure reactive impedance.

the configuration very complicated. Here we propose a unique solution in which, by modulating each side of the antenna platform, one can scan the beam as desired and electronically, while the configuration is simple and favorable for integration.

The configuration of such a leaky-wave antenna is depicted in Fig. 1 with the tunable material considered to be graphene. We need to emphasize that the concept is general and can be easily extended to any other thin-layer electrically tunable materials supporting plasmonic waves. In fact, by using proper tunable materials or 2-D sheets operating at other spectra, we can manage the design at desired optical frequencies. As observed in Fig. 1(a), a monolithic piece of grounded graphene without any pattern is put on top of the gate biasing strips with a thin layer of oxide in between. Biasing pad group A controls the direction of surface wave propagation in the $x-y$ plane. Pad group B provides sinusoidal impedance modulation, needed for generating leaky-wave radiation out of the antenna plane. Basically, the radiation in the ϕ direction is controlled by pad group A and in the θ direction by pad group B. The two groups of orthogonal and decoupled biasing allow for dynamic control of the beam radiation toward any desired 2-D direction, where the voltages can be simply applied on the two sides of the structure. The biasing configuration is significantly simplified compared to conventional pixel-by-pixel biasing. Of even more interest is that the proposed design provides not only beam direction scanning, but also dynamic control of the beamwidth. The electrical control can happen at nanosecond time scales and even faster [16], which shows exciting potential for the development of ultrafast optoelectronic devices.

2. DESIGN PRINCIPLES

A. Phase-Matching Condition

First, the concept of achieving 2-D radiation beam by 1-D impedance modulation is schematically explained using the phase-matching condition, as illustrated in Fig. 2. Consider beam scanning in just the elevation plane, as studied in [15]. In this case, excitation is a plane wave along the x axis, which has a surface wave vector $\vec{k}_{\text{sp}} = k_{\text{sp}}\hat{x}$. The sinusoidal modulation along the propagation direction gives rise to a group of effective wave vectors $\vec{k}_{\text{eff}} = 2\pi n/p\hat{x}(n = \pm 1, \pm 2, \pm 3\ldots$, and p is the modulation period). The superposition of $\vec{k}_{\text{sp}}$ with one effective wave vector, usually $\vec{k}_{\text{eff}} = -2\pi/p\hat{x}$, matches the azimuth plane projection of the radiated wave vector $\vec{k}_0$. In Fig. 2(a), the superposition of $\vec{k}_{\text{sp}}$ and $\vec{k}_{\text{eff}}$ is along the $\pm x$ direction. Thus, the radiation direction is always in the $x-z$ plane.

Nonetheless, if the surface wave vector is not along the x direction but has an angle α relative to the x axis, while keeping the sinusoidal modulation and, therefore, the effective wave vector in the same direction, the superimposed wave vector may point to any direction in the $x-y$ plane, not limited to be along x. As can be observed from Fig. 2(b), the phase-matching condition will transform the radiated beam to the plane composed by the superimposed vector and the z axis. This presents an interesting way to realize beam scanning in both the θ and ϕ directions but using only 1-D sinusoidal impedance modulation. The direction of the surface wave can be controlled by a beam tilter using proper 1-D impedance distribution along the direction perpendicular to the propagation. Note that the two types of impedance modulation are not related to each other, but both of them can be implemented by putting 1-D gating pads underneath graphene, taking advantage of its voltage-controllable conductivity. Gating pad group A in Fig. 1(a) is used to control the surface wave propagation direction α, by providing monotonically varied impedance in Fig. 1(b) to tilt the surface wave front. Pad group B provides the sinusoidal impedance modulation, as shown in Fig. 1(c). Such a configuration significantly reduces the complexity of gate biasing, which is of great promise for fabrication compared to pixel-by-pixel biasing.

A similar concept has already been used in the phased array of leaky-wave parallel line sources and optical phased arrays with phase-tuned channels for 2-D beam scanning in the

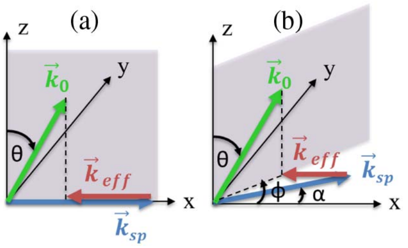

Fig. 2. (a) Phase matching for 1-D leaky-wave radiation with 1-D sinusoidal modulation. (b) Phase matching for 2-D leaky-wave radiation with 1-D sinusoidal modulation. $\vec{k}_{\text{sp}}$ is the unmodulated surface wave vector. $\vec{k}_{\text{eff}}$ is the effective wave vector from the periodic modulation. $\vec{k}_0$ is the radiating wave vector.

millimeter and infrared regimes [9,17,18]. Each line source or waveguide channel scans the beam in elevation by varying frequency. Phase shifters, in the form of resistive heating elements or phase delay lines, are incorporated in each channel to enable the scan in the azimuth plane. In such a way, the radiation is still a pencil beam, but toward the 2-D direction. The reported beam-scanning direction is narrowed to a small window, not the entire space, due to the limited number of channels and restricted phase tuning range. In contrast, the design in Fig. 1(a) is much more compact and powerful. Extra phase shifters are avoided, and replaced by simple biasing pad group A underneath the graphene. The azimuth scan is accomplished merely through tilting the surface wave. An elevation scan does not rely on frequency sweeping, so that one has the freedom to choose the frequency for a specific beam scan. The problem of crosstalk does not exist, as no channels are needed in the design. Instead, a piece of graphene sheet supports any beam radiation with appropriate electrical control.

B. Hologram Theory

To explore the analytical relation among the radiation direction $[\theta, \phi]$, surface wave direction α, and the impedance modulation, we employ a holographic design technique [19–21], which records the interference pattern of the guided surface wave and the desired radiated wave. One can design the holographic surface to be proportional to such interference pattern by modifying the quantities related to the surface, such as thickness, refractive index, and surface impedance. Here we design a surface-impedance-modulated holographic surface, because the surface impedance can be adjusted dynamically by gate biasing in graphene.

Generally, a surface wave propagating along α direction in the $x-y$ plane follows the expression

$$\Psi_{\mathrm{surf}} \propto \exp[-jk_0 n_{\mathrm{sp}}(x \cos \alpha + y \sin \alpha)], \tag{1}$$

where n_{sp} is the effective refractive index of the surface wave without any modulation, and k_0 is the free-space wave vector. The radiated beam toward the $[\theta, \phi]$ direction follows the expression

$$\Psi_{\mathrm{rad}} \propto \exp[-jk_0(x \sin \theta \cos \phi + y \sin \theta \sin \phi + z \cos \theta)]. \tag{2}$$

The interference of the two waves at the $z = 0$ plane gives

$$\Psi_{\mathrm{rad}} \cdot \Psi^*_{\mathrm{surf}}\Big|_{z=0} \propto \exp\{-jk_0[x(\sin \theta \cos \phi - n_{\mathrm{sp}} \cos \alpha) + y(\sin \theta \sin \phi - n_{\mathrm{sp}} \sin \alpha)]\}. \tag{3}$$

To simplify the interference pattern into a 1-D shape, namely, uniform along the y direction, the second term of Eq. (3) should be zero, which determines the direction of surface wave propagation as

$$\alpha = \sin^{-1}\left(\frac{\sin \theta \sin \phi}{n_{\mathrm{sp}}}\right). \tag{4}$$

Then the interference pattern of Eq. (3) is simplified into a sinusoidal modulation along x with period determined by

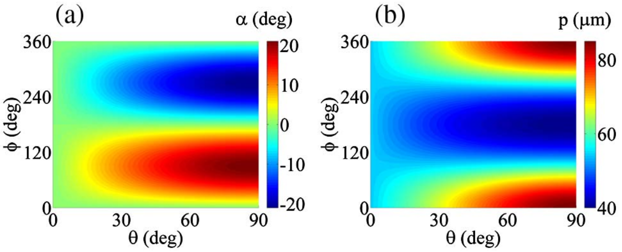

Fig. 3. (a) Surface wave propagating direction α and (b) sinusoidal modulation period p for any 2-D beam radiation $[\theta, \phi]$ when $n_{\mathrm{sp}} = 2.76$.

$$p = \frac{2\pi}{k_0(n_{\mathrm{sp}} \cos \alpha - \sin \theta \cos \phi)}. \tag{5}$$

By choosing the average impedance X_s and a modulation factor M, the impedance distribution X_{sB} realized by pad group B is the well-known formulation (assuming pure reactive surface impedance) [22,23]

$$X_{sB}(x) = X_s\left[1 + M \sin\left(\frac{2\pi x}{p}\right)\right]. \tag{6}$$

Furthermore, Fig. 3 presents the relations between $[\theta, \phi]$ and $[\alpha, p]$ when $n_{\mathrm{sp}} = 2.76$, which can be used to design a radiation beam that can be pointed to any arbitrary direction. This n_{sp} corresponds to the averaged surface impedance X_s of 977 Ω, as $X_s = \eta_0\sqrt{n_{\mathrm{sp}}^2 - 1}$, where η_0 is the free-space impedance. In this case, the range of the surface wave direction (α) is only from −20° to 20° to enable the complete radiation direction scan [360° in the azimuth plane (ϕ) and 90° in the elevation plane (θ)]. This is due to the high confinement of the graphene surface wave, according to Eq. (4). If a larger value of n_{sp} is used, the required range of the surface wave direction can even be reduced. Such a limited range of α can be easily achieved by properly biasing the profile from pad group A of Fig. 1(a).

Specifically, a linear index distribution is needed from pad group A to tilt the surface wave, which leads to monotonically varied surface impedance along the y axis, as illustrated in Fig. 1(b). Since the refractive index and the surface impedance are related to each other, the surface impedance distribution provided by pad group A can be determined as

$$X_{sA}(y) = \eta_0\sqrt{\left(n_0 + \frac{n_{\mathrm{sp}} y \sin \alpha}{l}\right)^2 - 1} \tag{7}$$

based on the geometric optics approximation [24]. n_0 is the starting point of the index, which can be chosen properly based on the available index range when gate biasing is applied, and l is the length of pad group A along the propagation direction.

To realize beam radiation toward a specific set of angles $[\theta, \phi]$, one can find the surface wave direction α and the modulation period p from Fig. 3. Then the impedance profiles above pad groups A and B are readily obtained using Eqs. (7) and (6). Such impedance profiles can be quickly reconfigured by dynamically changing α and p through gate biasing to shift the beam to a different direction.

3. NUMERICAL RESULTS AND DISCUSSION

Next we proceed to numerically validate such reconfigurable 2-D beam scanning using the finite-difference time-domain (FDTD) technique. The conductivity of graphene is modeled by the simplified Kubo formalism [15,25], which includes only the intraband contribution:

$$\sigma = -j\frac{e^2 K_B T}{\pi\hbar^2(\omega - j/\tau)}\left[\frac{\mu_c}{K_B T} + 2\ \ln\left(e^{-\frac{\mu_c}{K_B T}} + 1\right)\right], \quad \textbf{(8)}$$

where e is the elementary charge, K_B is the Boltzmann's constant, T is temperature, $\hbar$ is the reduced Planck constant, μ_c is the chemical potential, and τ is the relaxation time. Such simplification is accurate considering the working frequency of 2 THz and the limited voltage tuning range in this work. Realistic relaxation time τ of 1 ps is assumed at room temperature based on the measured electron mobility of graphene [26]. Gating pads can be placed underneath graphene to dynamically modify its local chemical potential with a thin spacer layer of SiO_2 in between. The relation between the chemical potential and the applied gate voltage can be accurately retrieved for a given thickness of the spacer layer based on the capacitor approximation [15,27,28]. However, considering that the gating pads are very thin with permittivity close to the SiO_2 substrate [15], we do not model them in the simulations. Instead, we consider the proper chemical potential for each portion of the graphene sheet corresponding to each gating pad. In addition, a uniform SiO_2 substrate with the thickness $h = 60$ μm and the permittivity of 3.8 is grounded by metal.

Variation of the surface impedance of the proposed structure as a function of the chemical potential of graphene has been analytically expressed in [15], based on a dispersion relation analysis. The resistance is small and not sensitive to chemical potential. Thus, only the reactance is used in the designs. However, the numerical model includes contributions from the total impedance. Variation of the surface reactance with graphene's chemical potential as reported in [15] can be represented as the following numerical fitting:

$$X = 313.7\left(\frac{\mu_c}{e}\right)^{-1.2} + 460, \quad \textbf{(9)}$$

which is valid for chemical potential from 0.2 to 0.9 eV. In this case, the surface reactance shows a large dynamic range from 2633 to 824 Ω.

The impedance profile from Eqs. (6) and (7) for any radiation direction can be interpreted as a chemical potential profile, and further as a voltage profile of pad groups A and B. In the simulation, the chemical potential profile is used and transformed into the proper conductivity for each portion of the graphene layer. The surface wave tilting area and the sinusoidally modulated area in graphene are represented by zones A and B for simplicity, in accordance with the definition of the gating pads in reality. Graphene is discretized into 10 μm wide strips in zone A and 1 μm wide strips in zone B, corresponding to pad widths of 10 and 1 μm in practice. The pad width of 10 μm in zone A is around 1/6 of the surface wavelength, which is fine enough to achieve any surface wave tilting angle α. The pad width of 1 μm in zone B is small enough to approach almost all the modulation periods p in Fig. 3(b).

A. Two-Dimensional Beam Scanning

As an example, we first design the beam radiation toward $[\theta, \phi] = [30°, 45°]$. According to Eqs. (4) and (5), the surface wave direction is calculated as $\alpha = 7.35°$, and the sinusoidal modulation period is $p = 62.86$ μm. The average impedance of the sinusoidal modulation is chosen as $Xs = 977\ \Omega$, corresponding to the refractive index $n_{\mathrm{sp}} = 2.76$ for the surface wave, the same as in Fig. 3. Modulation factor of $M = 0.13$ is selected. We set the length of graphene zone A along x to be $l = 100$ μm. The starting refractive index in zone A is selected to be $n_0 = 2.41$ to maximize the impedance overlap between zones A and B for the best impedance match. Taking all of the above parameters into account, we model the conductivity distribution for graphene in two zones. The size of the whole structure is 3.33λ along x and 4λ along y, where λ is the free-space wavelength at the designed frequency of 2 THz. An array of dipole sources with E_x polarization is positioned before zone A to excite the surface plane wave. Figures 4(a) and 4(b) provide information about the surface impedance distribution for such a design and the near-field distribution (real$\{E_x\}$) above the graphene surface. Surface wave tilting is obvious due to the monotonic impedance variation along y in zone A, which is crucial for beam radiation in the azimuth plane. In zone B of the impedance profile, around six periods of sinusoidal impedance modulation are modeled, so that most of the power is radiated and dissipated by the end of the structure. The effective refractive index estimated from the near-field plot in Fig. 4(b) is 2.81, which is very close to the average index of 2.76. One may notice that the amplitude is not uniform along the equiphase plane. This is because of the different coupling efficiency from the dipole source to the surface wave in the impedance-varying zone A.

To obtain the radiation pattern from the simulation, one should read the tangential near-field components on a closed box surrounding the structure, and convert them into the far-field radiation pattern through near-to-far field transformation. For the structure proposed in Fig. 1(a), there is no field on the backside because of the metal. The field is fairly weak in the substrate, and is mainly concentrated around the graphene layer. Therefore, only the near field on top of the structure is recorded and used to calculate the radiation pattern. This method has been proven to be efficient, yet accurate enough by comparing with the result obtained from the closed box. In addition, the dipole array is placed right at the beginning of zone A. Such excitation is not realistic. Part of the source energy is directly radiated into the space without coupling into the surface wave. This will degrade the radiation pattern of the leaky-wave antenna. In practice, such an issue would not come up in practical applications by using the excitation far away from the structure or using waveguide feeding. However, doing this here will increase the simulation burden significantly, and is not the focus of this work. Thus, we still keep the source close to the structure, and read the near-field twice, with and without the sinusoidal modulation. The subtraction between the two near fields, called the scattered field, will remove the effect of the source itself. The scattered field for the design of

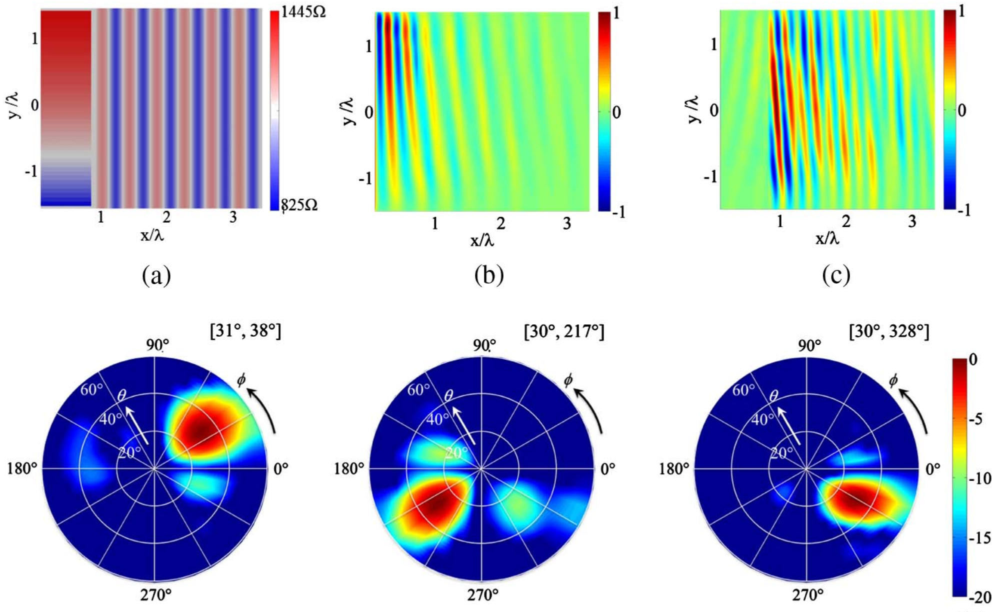

(a) (b) (c)

(d) (e) (f)

Fig. 4. (a) Surface impedance profile of the antenna structure for beam radiation to $[\theta, \phi] = [30°, 45°]$. The gradient impedance profile along y is for tilting the surface beam direction and the sinusoidal variation along x for leaking the wave. (b) Near-field distribution (real$\{E_x\}$) for the total field on top of the antenna structure. The beam tilting is obvious. (c) Near-field distribution for the scattered field in the same position as (b). (d) Radiation pattern from the graphene leaky-wave antenna when the designed beam radiation is $[\theta, \phi] = [30°, 45°]$. The beam direction from FDTD simulation is [30°, 40°]. (e) and (f) Radiation patterns for designed beam radiation toward [40°, 225°] and [30°, 330°]. The simulated beam directions are [40°, 220°] and [30°, 328°]. The color bar at the end is for (d) to (f). The fields in (b) and (c) are self-normalized.

Fig. 4(a) is plotted in Fig. 4(c), which relates to the far-field radiation pattern by Fourier transform. The scattered field is concentrated in zone B, as the field in zone A is purely a guided surface wave, and does not directly contribute to radiation. Based on Fig. 4(c), the far-field radiation pattern is calculated and indicated in Fig. 4(d). The radiation direction is measured as [30°, 40°], which is in good agreement with the design, considering the discretization of the conductivity distribution and the finite antenna size.

Following the same rule, beam radiation toward [40°, 225°] and [30°, 330°] is designed to show the dynamic beam-scanning capability in Figs. 4(e) and 4(f). In Fig. 4(e), the surface wave direction and the modulation period are evaluated to be $\alpha = -9.47°$ and $p = 47.16$ μm, while in Fig. 4(f), $\alpha = -5.19°$ and $p = 64.32$ μm. The simulated radiation directions are [40°, 220°] and [30°, 328°], respectively, as marked in the upper right corner of each radiation pattern. It should be mentioned that the same structure is used in the designs shown in Figs. 4(d)–4(f). The only difference is the impedance distribution in zones A and B, which can be quickly reconfigured by 1-D gate biasing in practice. The different modulation periods for the three cases are achieved by repeating voltages for every 63, 47, and 64 pads along zone B for cases in Figs. 4(d)–4(f), respectively.

In the three designs above, the surface wave tilting angles α are very small, and the expressions for θ and ϕ, respectively, can be simplified from Eqs. (4) and (5) as

$$\theta = \sin^{-1}\left(n_{sp} - \frac{\lambda}{p}\right), \tag{10}$$

$$\phi = \tan^{-1}\left(\frac{n_{sp}\alpha}{n_{sp} - \lambda/p}\right). \tag{11}$$

Thus we conclude from Eqs. (10) and (11) that the sinusoidal modulation mainly determines θ, while the surface wave tilting and the sinusoidal modulation together are in charge of ϕ.

The beam-scanning resolution and spatial range are critical characterizations in practical applications. The pad width in group A is estimated to be around 1/6 of the surface wavelength, which is fine enough for beam tilting within 20° [29]. We consider α accurate, as one can apply exact voltages to achieve the required impedance distribution in Eq. (7). The resolutions for θ and ϕ are determined by the resolution of sinusoidal modulation period p. p is always an integer multiple of the pad width. If $\theta_1 (\phi_1)$ is realized by grouping N pads in a period, the next available angle $\theta_2 (\phi_2)$ corresponds to grouping $N \pm 1$ pads in a period. The resolutions ($|\theta_1 - \theta_2|$ and $|\phi_1 - \phi_2|$) are calculated to be around 2° for θ and 5° for ϕ around the beam directions in Figs. 4(d)–4(f), when the resolution of p is defined as 1 μm in this work. This explains the relatively large mismatch between designed and simulated ϕ. The resolution in radiation angles can be improved by using narrower pad widths. The scanning ranges of [0 360°] for ϕ and [0 40°] for θ have been proven with good performance in Fig. 4. From the observation of Fig. 3, moving to larger θ means that α and p each move to an extreme value (either maximum or minimum). α can achieve 20° easily, and p can goes to 80 and 40 μm by combining every 80 and 40 pads, respectively, in a period. The numerical discretization of the sinusoidal modulation is good enough even for the smallest p. The only limitation is that the effective aperture size perpendicular to the radiation direction becomes smaller as the beam scans toward the broadside direction, which will degrade scanning accuracy. In this study, the aperture size is eventually limited by the material loss of graphene. If one can further reduce the material loss, a larger beam-scanning range can be reached.

B. Dynamic Beamwidth Control

As is well known, the beamwidth is related to the size of the antenna aperture. The larger the aperture, the narrower the beamwidth. In our proposed leaky-wave antenna [Fig. 1(a)], the physical aperture size is fixed, but the effective aperture size of the antenna can be modulated in real time, which adds another degree of functionality to the designed configuration. The effective aperture size the y direction is controlled by excitation. A dipole array is used to launch the surface plane wave. By changing the size of the dipole array through turning on or off some sources, one may obtain different aperture sizes along y, which mainly determine the beamwidth in the azimuth plane. In practice, one may control the feeding array size, instead. The effective aperture size along x is how far the power is totally radiated into space and dissipated by the material loss, which specifies the beamwidth in the elevation plane. Ideally, leaky-wave antennas with high efficiency transfer most of the incident power from the guided mode into the radiation mode after a certain propagation distance, which is usually defined as the effective antenna length. A large modulation factor M will lead to a large leakage rate and small effective antenna length, and vice versa. Thus, tuning M is a good approach to controlling the beamwidth in the elevation plane, with negligible effect on the beam radiation angle if M is not very large.

Considering a graphene-based leaky-wave antenna, most of the power can be dissipated before it is all converted into radiation due to the electron scattering in graphene. The dissipation loss for graphene is larger than the leakage rate, as will be characterized in the following. It is not efficient to change the effective aperture size along x via dynamic control of M. Instead, one can change the dissipation loss by defining different average impedance X_s of the sinusoidal modulation. From Eq. (9), smaller X_s is achieved with larger chemical potential, which leads to smaller effective refractive index together with smaller dissipation loss. Once X_s is fixed, the surface wave propagation direction α and the sinusoidal modulation period p should be modified accordingly, based on Eqs. (4) and (5), to keep the same radiation direction. The benefit of the proposed structure is actually in controlling all the impedance-related parameters (α, X_s, M, p) dynamically and independently by simple variation of the biasing voltage.

Dynamic beamwidth control is investigated numerically for the case of beam radiation to [30°, 330°]. The physical antenna aperture size is fixed to be 3.9λ along x and 4.0λ along y. To realize a small effective aperture size, a dipole array with length of 2.0λ along y is used for excitation. The average impedance X_s is chosen to be 2300 Ω, corresponding to μ_c of 0.24 eV and the normalized dissipation loss $\alpha_{\mathrm{sp}}/k_0 = 0.45$. Modulation factor $M = 0.13$ gives normalized leakage rate $\alpha_{\mathrm{rad}}/k_0 = 0.0029$. Considering 95% power attenuation due to dissipation and leakage with the remaining 5% absorbed by a matched load [17], the effective length of the antenna along x is approximately 0.53λ. In contrast, for a large effective aperture, a dipole array with length of 4.0λ is used, and a small X_s of 977 Ω is chosen with $\mu_c = 0.66$ eV. The normalized dissipation loss and the leakage rate are evaluated to be $\alpha_{\mathrm{sp}}/k_0 = 0.12$ and $\alpha_{\mathrm{rad}}/k_0 = 0.0026$, respectively, for $M = 0.13$. The corresponding effective antenna length for 95% power attenuation is increased to 2λ. To steer the beam to the same direction of [30°, 330°], the surface wave direction is $\alpha = -2.33°$ for the small aperture case and $\alpha = -5.19°$ for the large aperture case; the modulation periods are 26.1 and 64.3 μm, respectively.

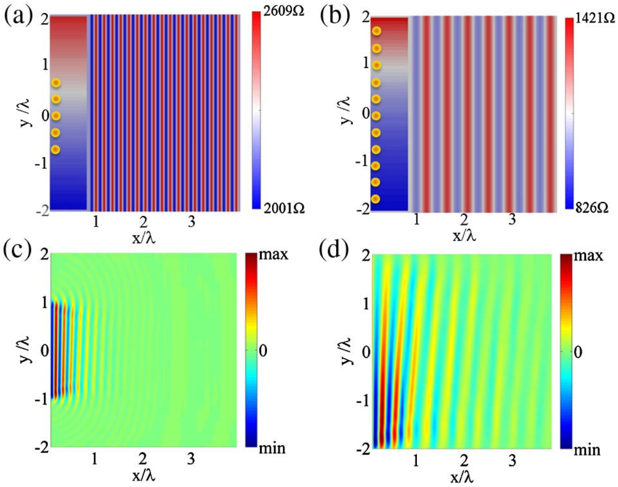

Fig. 5. (a) Impedance profile leading to a small effective aperture size for beam radiation to [30°, 330°]. (b) Impedance profile leading to a large effective aperture size for beam radiation to [30°, 330°]. The dipole arrays are shown in (a) and (b) at the beginning of zone A with different array sizes as the excitation sources. (c) and (d) Near-field distributions of the total field (Re$\{E_x\}$) above graphene corresponding to (a) and (b), respectively, which show large differences in the effective aperture size.

The surface impedance profiles for the two cases are illustrated in Figs. 5(a) and 5(b). The physical sizes are exactly the same. The only difference is the different impedance profiles in zones A and B, which can be regenerated quickly through voltage control. The dipole array is illustrated at the beginning of zone A for both cases. The near-field distribution above the graphene layer for the designs in Figs. 5(a) and 5(b) are shown in Figs. 5(c) and 5(d). The change of the effective aperture size is obvious along both the x and y directions. The 2-D radiation patterns are shown in Figs. 6(a) and 6(b) for the small and the large effective aperture designs, respectively. And Figs. 6(c) and 6(d) compare the radiation pattern in the ϕ plane and the θ plane for the two designs. From the small effective aperture to the large one, the 3 dB beamwidth is tuned from 43° to 28° along ϕ, and from 37° to 19° along θ. Further increasing the physical aperture size does not help to narrow the beamwidth, as the energy is totally dissipated. The beamwidth is finally limited by the material loss from graphene. A relaxation time of longer than 1 ps has been observed [30], which helps to

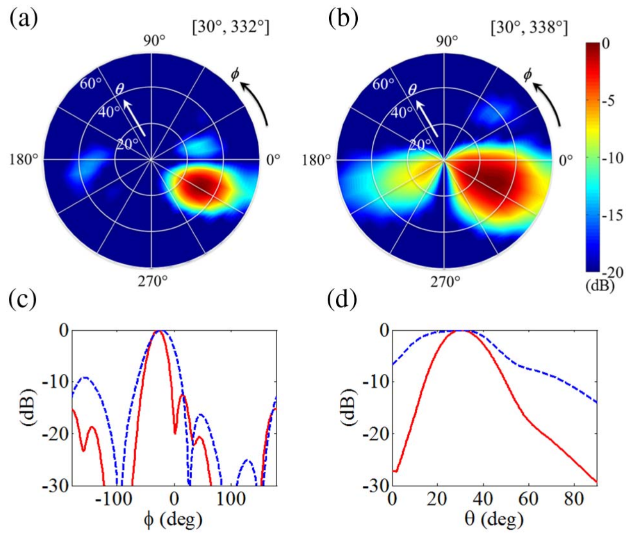

Fig. 6. (a) and (b) 2-D radiation patterns for the designs in Figs. 5(a) and 5(b), respectively. (c) Radiation patterns in the ϕ plane. The blue dashed line is from (a) and the red solid line is from (b). The 3 dB beamwidths for ϕ are 43° and 28°, respectively. (d) Radiation patterns in the θ plane for (a) (blue dashed line) and (b) (red solid line). The 3 dB beamwidths for θ are measured to be 37° and 19°, respectively.

further narrow the beamwidth and increase the directivity with a larger physical aperture size.

By taking advantage of discrete voltage control, both X_s and M can be modulated in real time by applying the proper voltage distribution without any change to the configuration. Dynamic tuning of the two parameters provides control of dissipation loss and leakage rate, respectively. The best solution of beamwidth shaping is to change M if the gate-tunable material has low loss, i.e., a pure reactive impedance surface. However, considering the available graphene quality, we controlled the alternative parameter X_s. A small modulation factor M is chosen for all the designs here, hence the radiation efficiency of such an antenna [15] will reach a few percent (about 2%) for the narrow beamwidth design in Fig. 5. A larger modulation factor M of about 0.35 can be used as in [15] to manage a larger efficiency of around 10%. The efficiency can be further increased by reducing the dissipation loss with other fabrication techniques, such as encapsulating graphene with boron nitride layers, while keeping the electrically tunable feature [31]. The proposed concept is general and can be applied to other tunable materials (not just graphene).

4. CONCLUSION

In summary, a leaky-wave antenna is proposed for 2-D beam scanning with 1-D electrical controls on the sides of the structure. Both beam direction and beamwidth are dynamically tuned. Sinusoidal impedance modulation along the surface wave propagation scans the beam along the elevation plane by changing the modulation period. Orthogonal monotonic impedance modulation at the feeding end scans the beam along the azimuth plane by providing the proper phase shift for feeding. The gate-tunable property of graphene naturally combines the two types of modulation and makes the reconfiguration quite simple and fast within the extremely compact structure. This concept is not limited to graphene-based designs, but can be applied to any gate-tunable 2-D sheet or thin film. Utilizing proper gate-tunable materials (other than graphene) can allow for operation at other desired optical frequencies, and can further lead to less plasmonic loss. The proposed concept can even be extended to temperature-sensitive structures, as local temperature control is also attained through electrical connections to the local heaters. This work may provide far-reaching applications in low-cost and compact reconfigurable optoelectronic components.

Funding. Air Force Office of Scientific Research (AFOSR) (FA9550-14-1-0349); Army Research Office (ARO) (MURI Award W911NF-14-0247).

REFERENCES

1. D. Tse and P. Viswanath, *Fundamentals of Wireless Communication* (Cambridge University, 2005).
2. C. A. Balanis, *Antenna Theory: Analysis and Design* (Wiley-Interscience, 2005).
3. S. V. Hum, M. Okoniewski, and R. J. Davies, “Modeling and design of electronically tunable reflect arrays,” IEEE Trans. Antennas Propag. **55**, 2200–2210 (2007).
4. H. Kamoda, T. Iwasaki, J. Tsumochi, T. Kuki, and O. Hashimoto, “60-GHz electronically reconfigurable large reflect array using single-bit phase shifters,” IEEE Trans. Antennas Propag. **59**, 2524–2531 (2011).
5. S. V. Hum and J. Perruisseau-Carrier, “Reconfigurable reflect arrays and array lenses for dynamic antenna beam control: a review,” IEEE Trans. Antennas Propag. **62**, 183–198 (2014).
6. Y. C. Jun, E. Gonzales, J. L. Reno, E. A. Shaner, A. Gabbay, and I. Brener, “Active tuning of mid-infrared metamaterials by electrical control of carrier densities,” Opt. Express **20**, 1903–1911 (2012).
7. V. W. Brar, M. S. Jang, M. Sherrott, J. J. Lopez, and H. A. Atwater, “Highly confined tunable mid-infrared plasmonics in graphene nanoresonators,” Nano Lett. **13**, 2541–2547 (2013).
8. J. Sun, E. Timurdogan, A. Yaacobi, E. S. Hosseini, and M. R. Watts, “Large-scale nanophotonic phased array,” Nature **493**, 195–199 (2013).
9. J. K. Doylend, M. J. R. Heck, J. T. Bovington, J. D. Peters, L. A. Coldren, and J. E. Bowers, “Two-dimensional free-space beam steering with an optical phased array on silicon-on-insulator,” Opt. Express **19**, 21595–21604 (2011).
10. Y.-J. Yu, Y. Zhao, S. Ryu, L. E. Brus, K. S. Kim, and P. Kim, “Tuning the graphene work function by electric field effect,” Nano Lett. **9**, 3430–3434 (2009).
11. F. Wang, Y. Zhang, C. Tian, C. Girit, A. Zettl, M. Crommie, and Y. R. Shen, “Gate-variable optical transitions in graphene,” Science **320**, 206–209 (2008).
12. T. Driscoll, H.-T. Kim, B.-G. Chae, B.-J. Kim, Y.-W. Lee, N. M. Jokerst, S. Palit, D. R. Smith, M. Di Ventra, and D. N. Basov, “Memory metamaterials,” Science **325**, 1518–1521 (2009).
13. Z. You, C. Xiaonan, K. Changhyun, Y. Zheng, C. Mouli, and S. Ramanathan, “Voltage-triggered ultrafast phase transition in vanadium dioxide switches,” IEEE Electron Device Lett. **34**, 220–222 (2013).
14. E. Feigenbaum, K. Diest, and H. A. Atwater, “Unity-order index change in transparent conducting oxides at visible frequencies,” Nano Lett. **10**, 2111–2116 (2010).
15. M. Esquius-Morote, J. S. Gomez-Diaz, and J. Perruisseau-Carrier, “Sinusoidally modulated graphene leaky-wave antenna for electronic beam scanning at THz,” IEEE Trans. Terahertz Sci. Technol. **4**, 116–122 (2014).

16. M. Liu, X. Yin, E. Ulin-Avila, B. Geng, T. Zentgraf, L. Ju, F. Wang, and X. Zhang, "A graphene-based broadband optical modulator," Nature **474**, 64–67 (2011).
17. J. Volakis, *Antenna Engineering Handbook* (McGraw-Hill, 2007).
18. P. Lampariello and A. A. Oliner, "A novel phased array of printed-circuit leaky-wave line sources," in *17th European Microwave Conference* (1987), pp. 555–560.
19. M. ElSherbiny, A. E. Fathy, A. Rosen, G. Ayers, and S. M. Perlow, "Holographic antenna concept, analysis, and parameters," IEEE Trans. Antennas Propag. **52**, 830–839 (2004).
20. B. H. Fong, J. S. Colburn, J. J. Ottusch, J. L. Visher, and D. F. Sievenpiper, "Scalar and tensor holographic artificial impedance surfaces," IEEE Trans. Antennas Propag. **58**, 3212–3221 (2010).
21. M. Farmahini-Farahani and H. Mosallaei, "Functional-graded index metasurfaces for infrared radiation and guiding," IEEE Trans. Nanotechnol. **14**, 75–81 (2015).
22. A. A. Oliner and A. Hessel, "Guided waves on sinusoidally-modulated reactance surfaces," IEEE Trans. Antennas Propag. **7**, 201–208 (1959).
23. A. M. Patel and A. Grbic, "A printed leaky-wave antenna based on a sinusoidally-modulated reactance surface," IEEE Trans. Antennas Propag. **59**, 2087–2096 (2011).
24. J. Neu, R. Beigang, and M. Rahm, "Metamaterial-based gradient index beam steerers for terahertz radiation," Appl. Phys. Lett. **103**, 041109 (2013).
25. G. W. Hanson, "Dyadic Green's functions for an anisotropic, non-local model of biased graphene," IEEE Trans. Antennas Propag. **56**, 747–757 (2008).
26. C. R. Dean, A. F. Young, I. Meric, C. Lee, L. Wang, S. Sorgenfrei, K. Watanabe, T. Taniguchi, P. Kim, K. L. Shepard, and J. Hone, "Boron nitride substrates for high-quality graphene electronics," Nat. Nanotechnol. **5**, 722–726 (2010).
27. W. Gao, J. Shu, C. Qiu, and Q. Xu, "Excitation of plasmonic waves in graphene by guided-mode resonances," ACS Nano **6**, 7806–7813 (2012).
28. J. Xia, F. Chen, J. Li, and N. Tao, "Measurement of the quantum capacitance of graphene," Nat. Nanotechnol. **4**, 505–509 (2009).
29. N. Yu, P. Genevet, M. A. Kats, F. Aieta, J. Tetienne, F. Capasso, and Z. Gaburro, "Light propagation with phase discontinuities: generalized laws of reflection and refraction," Science **334**, 333–337 (2011).
30. K. I. Bolotin, K. J. Sikes, Z. Jiang, M. Klima, G. Fudenberg, J. Hone, P. Kim, and H. L. Stormer, "Ultrahigh electron mobility in suspended graphene," Solid State Commun. **146**, 351–355 (2008).
31. A. Woessner, M. B. Lundeberg, Y. Gao, A. Principi, P. Alonso-Gonzalez, M. Carrega, K. Watanabe, T. Taniguchi, G. Vignale, M. Polini, J. Hone, R. Hillenbrand, and F. H. L. Koppens, "Highly confined low-loss plasmons in graphene-boron nitride heterostructures," Nat. Mater. **14**, 421–425 (2015).